Coincidence-Site-Lattice Twist Boundaries in Bicrystalline α-Fe$_2$O$_3$ Nanoblades

Yiqian Wang,*,[†] Chao Wang,[†] Lu Yuan,[‡] Rongsheng Cai,[†] Xuehua Liu,[†,§] Chunyan Li,[†] and Guangwen Zhou[‡]
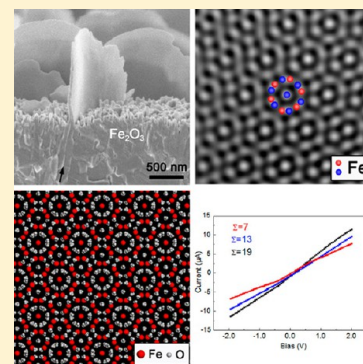
[†]The Cultivation Base for State Key Laboratory, Qingdao University, No. 308 Ningxia Road, Qingdao 266071, P. R. China

[‡]Department of Mechanical Engineering & Multidisciplinary Program in Materials Science and Engineering, State University of New York, Binghamton, New York 13902, United States

[§]Laboratory of Advanced Materials and Electron Microscopy, Institute of Physics, Chinese Academy of Sciences, Beijing 100080, P. R. China

S *Supporting Information*

ABSTRACT: Bicrystals are usually artificially designed to correlate the coincidence-site-lattice (CSL) configurations with the grain boundary property. Here, we report on CSL twist boundaries in bicrystalline α-Fe$_2$O$_3$ nanoblades, possessing only three distinct Σ values of 7, 13, and 19. The existence of CSL boundaries with various Σ values in the two-dimensional (2D) α-Fe$_2$O$_3$ nanoblades provides a good opportunity to investigate the effects of different grain boundaries on their physical properties. It is shown that the electrical resistivity of individual nanoblade decreases with increasing Σ values of the CSL boundaries. Such 2D nanoblades may have practical appeal because their 2D geometries facilitate integration into devices with realistic pathways to manufacturing.

1. INTRODUCTION

Grain boundary engineering (GBE) is a technique for optimizing the population of special grain boundaries in an effort to improve component material performance.[1−3] Coincidence-site-lattice (CSL) boundaries, in either pure twist or tilt boundary alignment, which are usually described by the parameter Σ, have demonstrated desirable properties such as ranging from low intrinsic electrical resistivity, great resistance to grain boundary fracture and cavitation, and to the initiation of localized corrosion.[4] The importance of such boundaries was first realized by Kronberg and Wilson in 1949,[5] and then significant research work has been conducted with an attempt to produce high fractions of CSL boundaries in polycrystalline metals,[6] metallic alloys,[7,8] and ceramics[9] in order to improve their mechanical properties. Recent studies[10−12] have shown that CSL boundaries can also exist in polycrystalline graphene which is a hexagonal, two-dimensional crystal of carbon atoms, and its mechanical and electronic properties are greatly influenced by these special boundaries. However, in polycrystals, grain boundaries rarely have an exact CSL configuration, and the link between grain boundary geometry and properties is very complicated due to the coupling of different boundary structures. To correlate individual CSL boundary with its physical property, previous studies have been performed on hexagonal close-packed (hcp) ZnO bicrystals with CSL boundaries formed by welding two single crystals together face-to-face at predetermined misorientations.[13,14] The

advantage of such process is that the crystallography of grain boundaries can be carefully controlled, and the interface between the bicrystals can be prepared as tilt or twist boundaries. However, these bicrystals are artificially designed to acquire desired orientations.

Bicrystalline α-Fe$_2$O$_3$ nanowires have been synthesized by thermal oxidation of iron (Fe) foils in an oxygen-containing atmosphere.[15] Through modifying the surface roughness of Fe foils by a sandblasting process, morphologies of hematite nanostructures transformed from nanowires into nanoblades.[16] Here we show that these nanoblades naturally grow as bicrystals with twist grain boundaries. Extensive transmission electron microscopy (TEM) observations demonstrate that these bicrystalline α-Fe$_2$O$_3$ nanoblades possess [0001] twist boundaries with only three distinct Σ values of 7, 13, and 19, where Σ is a value defined as the reciprocal density of coincident sites at the grain boundary between two adjoining grains in the framework of CSL model.[5] For example, if the Σ value is 7, it means that 1/7 of the atoms of the new orientation are coincident with the atoms of the old orientation. A simple geometric pattern is used to describe the rotation angles leading to the formation of the CSL twist boundaries for rotations about [0001] in hcp crystals. The electrical properties of

individual α-Fe$_2$O$_3$ nanoblades are investigated to correlate with the CSL boundary configurations.

2. EXPERIMENTAL SECTION

2.1. Sample Preparation. High-purity Fe foils (99.99%) with a thickness of 250 μm obtained from Sigma-Aldrich were used in the oxidation experiments. The Fe foils were first sandblasted by glass bead abrasives with diameters ranging from 150 to 250 μm for 9 s at the pressure of 100 psi to modify the surface morphology and roughness. The sandblasted samples were then thoroughly rinsed with deionized water followed by ultrasonication in acetone for 5 min. The cleaned Fe substrates were dried in N$_2$ and then placed on a substrate heater in a vacuum chamber and the sample temperature was monitored using a K-type thermocouple in contact with the substrate heater. The oxidation chamber was first pumped to vacuum of 2×10^{-6} Torr and then filled with 300 mbar oxygen pressure (the purity of oxygen is 99.999%). The chamber was then sealed and the Fe samples were heated to 600 °C at a rate of 20 °C/min and oxidized at 600 °C for 1 h. It was then cooled down in the same oxygen atmosphere to room temperature at a rate of 10 °C/min. The yield of Fe$_2$O$_3$ nanoblades can be controlled by adjusting the dimensions of Fe foils.

2.2. Characterization. The surface morphologies and crystal structures of the oxidized samples were examined using FEI Supra 55VP field-emission scanning electron microscope (SEM) and X-ray diffractometer (PANalytical's X'Pert). Cross-sectional specimens of oxidized Fe foils for TEM observations were prepared using conventional techniques of mechanical polishing and ion-thinning. The ion thinning was carried out using Gatan model 691 precision ion polishing system (PIPS). TEM samples of Fe$_2$O$_3$ nanoblades were prepared by peeling off the black products from the surface of oxidized Fe foils, then ultrasonicating them in ethanol for several minutes, and dispersing a drop onto a holey-carbon-film-coated copper grid. Selected-area electron diffraction (SAED), bright-field (BF) imaging, and high-resolution transmission electron microscopy (HRTEM) observations were carried out using a JEOL JEM 2100F TEM operated at 200 kV. Electron energy-loss spectroscopy (EELS) was performed on a Tecnai F20 TEM. The HRTEM image simulations were carried out using the xHREM software.

2.3. Electrical Properties. The electrical properties of an individual nanoblade was investigated using an *in situ* TEM sample holder (FM 200E HA300) purchased from Sweden Nanofactory Company, specially designed to measure the electrical properties of nanomaterials. The as-prepared Fe$_2$O$_3$ nanoblades were first transported onto the tip of gold rod and then moved to touch the atomic force microscopy (AFM) sensor made of gold using the piezodriven manipulation holder inside the TEM. The applied bias voltage ranged from −5 to 5 V. A schematic diagram for *in situ* measurement of electrical property is shown in Figure S1.

3. RESULTS AND DISCUSSION

Figure 1a shows a top-view SEM image of the oxidized products, from which it can be seen that the nanoblades, like flower petals, cover on the entire surface of the oxidized Fe foil. X-ray diffraction (XRD) pattern (Figure S2) indicates that the nanoblades have a rhombohedral hematite structure. Figure 1b shows a typical cross-sectional SEM image of an individual nanoblade with dimensions of about 1 μm long and 500 nm
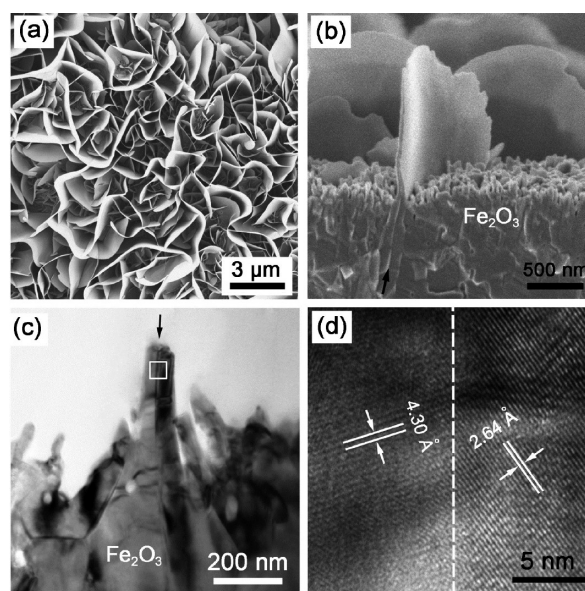

Figure 1. (a) Top-view SEM image of α-Fe$_2$O$_3$ nanoblades. (b) Cross-section SEM image of an individual nanoblade extruded from underneath oxide layers. (c) Cross-section BF TEM image of an individual nanoblade.[16] (d) HRTEM image of the nanoblade in (c).[16]

wide. The thickness of nanoblades decreases gradually from the bottom to the top. Our previous study[16] showed that Fe can be oxidized to produce Fe/FeO/Fe$_3$O$_4$/Fe$_2$O$_3$ (from bottom to top, oxide layer thickness about 12 μm) layered structure with hematite nanoblades grown on the top layer of Fe$_2$O$_3$. It is found that nanoblades are formed through the coalescence of two nanoislands during the oxidation process, possessing a bicrystal structure, which can be seen clearly in the cross-sectional BF TEM image (Figure 1c)[16] and HRTEM image (Figure 1d).[16] However, it is not feasible to determine the orientation relationship between the two crystals from the cross-sectional HRTEM images due to the tilting limit of the TEM sample holder and large magnetic field influence from the substrate.

To elucidate the exact orientation relationship between the two crystals forming the nanoblades, extensive planar-view TEM examinations were carried out on individual nanoblades dispersed on a holey-carbon-film-coated copper grid. It shows that all the nanoblades prefer to lie on the carbon film with [0001] axis oriented upright. It is found that most nanoblades (>95%) have a bicrystal structure, and the two crystals forming the nanoblades rotate against each other around the [0001] axis with only three distinct angles of 13.17°, 21.79°, and 27.80°, conforming to the rotation angles in CSL theory. All the boundaries in the bicrystalline nanoblades belong to CSL twist boundaries with corresponding Σ values of 19, 7 and 13, respectively. To give a reliable occurrence frequency for different CSL boundaries, more than 100 individual nanoblades are examined, and a statistical analysis is carried out. It shows that the Σ7 boundary has a volume fraction of 60%, Σ13 boundary possesses a volume percentage of 30%, and Σ19 boundary has a volume fraction of only 10%.

Figure 2 shows an example of a nanoblade with a Σ7 boundary. Figure 2a is a typical BF TEM image of an individual Fe$_2$O$_3$ nanoblade with a length of about 1.1 μm and a width of about 300 nm. The thickness of the nanoblade edge is determined to be 18 nm using EELS (Figure S3a). No other
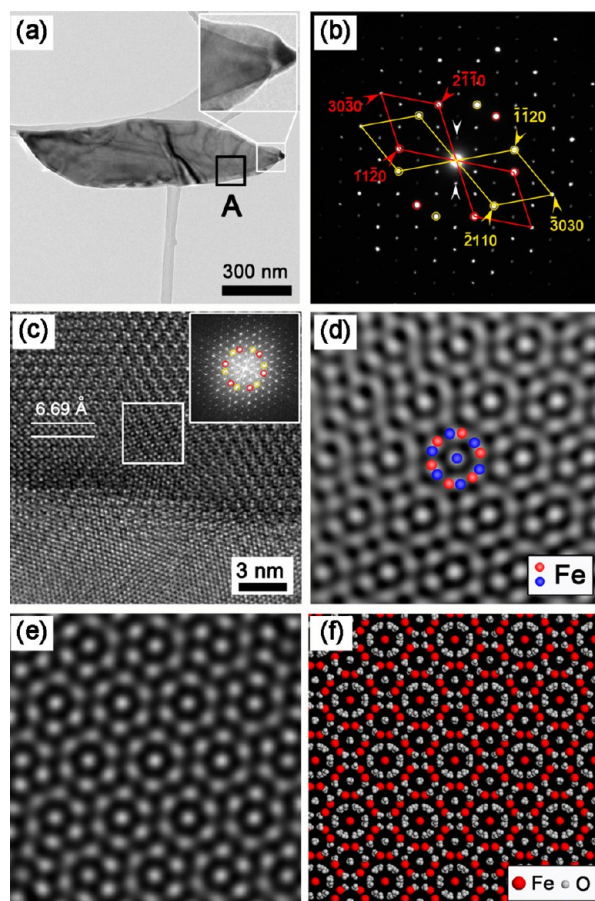
Figure 2. (a−c) BF TEM image, SAED pattern, and HRTEM image of α-Fe$_2$O$_3$ nanoblade with a $\Sigma 7$ CSL boundary. The inset in (a) is magnified image of rectangular region, and the inset in (c) corresponds to the FFT from the image in (c). (d) Fourier-filtered HRTEM image. (e) Simulated HRTEM image. (f) Atomic structural model of two superimposed (0001) α-Fe$_2$O$_3$ with a twist angle of 21.79°.

impurities can be detected from the EELS spectrum (Figure S3b). Careful examination of the nanoblade edge as seen in the inset of Figure 2a shows that the nanoblade is not a single-layer, but a double-layered structure. Figure 2b is an SAED pattern taken from the nanoblade in Figure 2a, containing two sets of [0001] zone-axis diffraction spots that can be indexed using the lattice parameters of α-Fe$_2$O$_3$ ($a = b = 5.028$ Å, $c = 13.730$ Å, $\alpha = 90°$, $\gamma = 120°$). These two sets of diffraction spots rotate against each other with a rotation angle of 21.79°. Thus, this nanoblade has a bicrystal structure, and the twist angle between the two layered crystals is 21.79°. In order to distinguish the two sets of the diffraction spots, one set is marked by yellow lines and the other is labeled by red lines. In addition to the fundamental diffraction spots, satellite spots also appear, as indicated by small white arrowheads in Figure 2b. Figure 2c shows a typical [0001] zone-axis HRTEM image from the α-Fe$_2$O$_3$ nanoblade edge as marked by a black rectangle in Figure 2a. This HRTEM image clearly shows two parts: the lower part is a single-layered lattice image of α-Fe$_2$O$_3$, and the upper part depicts Moiré fringes contrast formed by overlapping of double-layered crystal lattices. The distance between the Moiré fringes measured from the HRTEM image in Figure 2c is 6.69 Å, which agrees with the fringe spacing calculated from the satellite spots in the SAED pattern (Figure 2b). To

prove that the Moiré fringes result from the overlapping of two identical (0001) α-Fe$_2$O$_3$ crystals with a twist angle, the equation[17]

$$ d_m = \frac{d_1 d_2}{\sqrt{d_1^2 + d_2^2 - 2d_1 d_2 \cos\theta}} \tag{1} $$

is adopted to calculate the space (d_m) between Moiré fringes. In this equation, d_1 and d_2 are the lattice spacing of $\{11\bar{2}0\}$ planes of α-Fe$_2$O$_3$ ($d_1 = d_2 = 2.514$ Å), and θ is the twist angle ($\theta = 21.79°$). The calculated spacing d_m between the Moiré fringes is 6.65 Å, which is in good agreement with the measured value from the SAED pattern (Figure 2b) and the HRTEM image (Figure 2c). Therefore, the Moiré fringes in Figure 2c are produced by twisting two identical (0001) α-Fe$_2$O$_3$ crystals. If two identical crystals coalesce together by a pure twist, a boundary will naturally form. To investigate the nature of the boundary, we perform fast Fourier transform (FFT) analysis of the HRTEM image in Figure 2c. The original HRTEM image is reconstructed from the FFT pattern by filtering the selected spots. Figure 2d is the Fourier-filtered HRTEM image using the spots marked by circles in the inset of Figure 2c, where a superlattice structure is formed and its periodicity is consistent with the spacing between the Moiré fringes. The formation of such superlattice structure is attributed to the coincident sites at certain positions, which is further confirmed by the atomic structural model (Figure 2f) of two superimposed (0001) α-Fe$_2$O$_3$ with a twist angle of 21.79°. In Figure 2d,f, every coincident site is surrounded by 12 Fe atoms, so the Σ value for this CSL boundary is determined to be 7. To further clarify the superlattice structure in Figure 2d, systematic HRTEM simulations are carried out. The atomic model for the CSL boundary is illustrated in Figure S4a, and the simulated HRTEM images are demonstrated in Figures S5 and S6. When the defocus value is close to the experimental condition (45 nm), and the thickness of the specimen is similar to the real thickness of the nanoblade (18.76 nm), the simulated HRTEM image in Figure 2e agrees well with the Fourier-filtered HRTEM image in Figure 2d.

Figure 3 shows examples of another two individual nanoblades with $\Sigma 13$ and $\Sigma 19$ boundaries. TEM examinations show that these two nanoblades also have CSL boundaries arising from pure twist of two identical (0001) α-Fe$_2$O$_3$ crystals. The twist angle is determined to be 27.80° and 13.17° from the SAED patterns in Figures 3b and 3f, respectively. Moiré fringes can be clearly seen from Figures 3a and 3e with spacings of 9.51 and 9.83 Å, respectively. The periodicities for the superlattice structures are calculated to be 9.73 and 9.91 Å from Figures 3b and 3f, which are consistent with those measured from the HRTEM images. The Σ values are determined to be 13 and 19 from both the Fourier-filtered HRTEM images (Figures 3c and 3g) and atomic structural models (Figures 3d and 3h). To validate our analysis, systematic HRTEM simulations for [0001] zone-axis α-Fe$_2$O$_3$ are performed. The atomic model for the CSL boundary is illustrated in Figure S4b,c, and the simulated HRTEM images are demonstrated in Figures S7−S10. The simulated HRTEM images are consistent with our experimental observations.

Most observations on CSL boundaries have been focused on the bicrystals with tilt boundaries and are usually viewed along the boundary using TEM[13,18,19] because the two crystals have the same zone axes along the tilting axis. However, for bicrystals with twist boundaries, the zone axes of two crystals are different
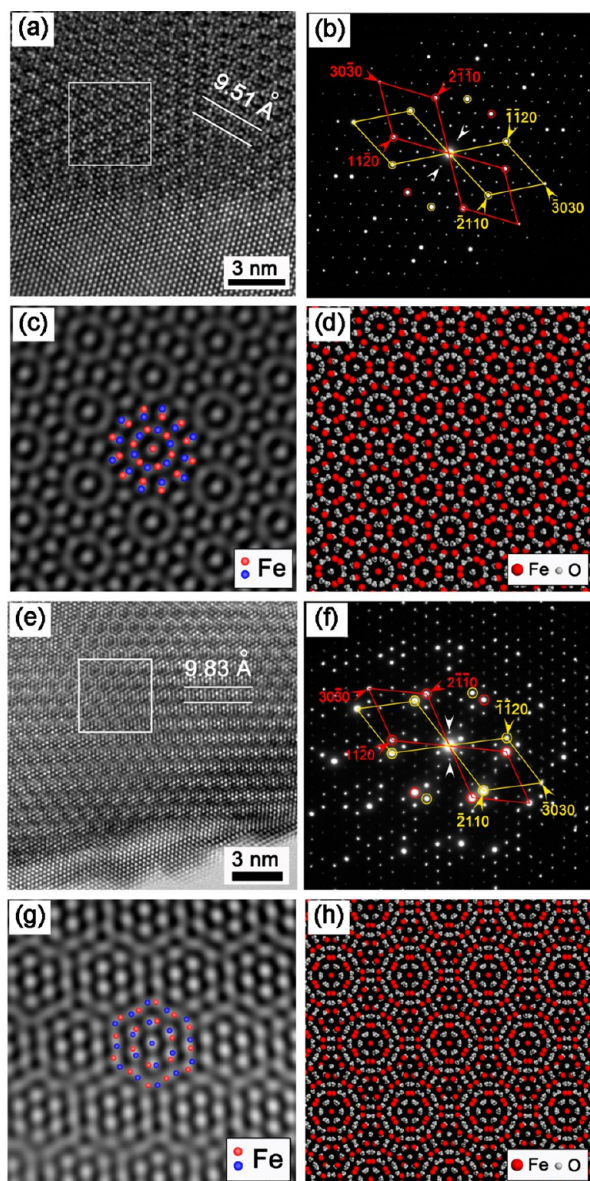
Figure 3. (a−d) Typical HRTEM image, SAED pattern, Fourier-filtered image, and atomic structural model of Fe_2O_3 nanoblade with a $\Sigma13$ CSL boundary. (e−h) Typical HRTEM image, SAED pattern, Fourier-filtered image, and atomic structural model of Fe_2O_3 nanoblade with a $\Sigma19$ CSL boundary.

along the boundary, so the ideal observation direction is perpendicular to the boundary. In the present work all the CSL twist boundaries in bicrystalline Fe_2O_3 nanoblades are viewed from the [0001] direction in order to clarify the orientation relationship between the two crystals. In addition, all the CSL boundaries mentioned above naturally occur in the α-Fe_2O_3 nanoblades during the oxidation process of sandblasted Fe foils. Such CSL boundaries have never been observed in any other nanomaterials. The formation of the CSL boundaries in the nanoblades might be related to the rough Fe surfaces caused by sandblasting and coalescence of adjacent oxide nanoislands.[16] For hcp systems, theoretical calculations showed that many kinds of CSL boundaries with different Σ values exist for the rotations around [0001].[20] However, in our case, only three distinct types of CSL boundaries are observed with Σ values of 7, 13, and 19, respectively. According to the CSL theory, these

three boundaries have the lowest interfacial energy because the Σ values are the lowest for rotations around [0001].[21]

Careful examination of the three SAED patterns demonstrates that all the main diffraction spots locate at the nodes of hexagonal network formed by satellite diffraction spots, and no extra diffraction spots arise from Fe or other iron oxides, as indicated in Figure 4a−c. Therefore, a simple geometric pattern
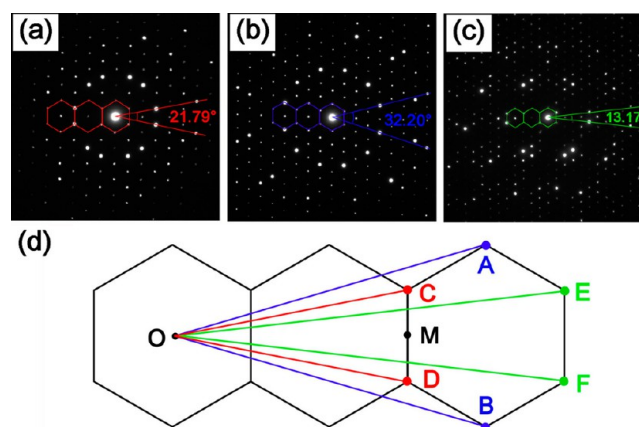

Figure 4. (a−c) SAED patterns obtained from the α-Fe_2O_3 nanoblades with rotation angles of 21.79°, 27.80°, and 13.17°. (d) Hexagonal network pattern demonstrating the twist angles between two identical (0001) Fe_2O_3 crystals.

(Figure 4d) composed of regular hexagons can be used to describe the rotation angles between two sets of main diffraction spots. The rotation of two Fe_2O_3 hexagon layers is demonstrated in Figure S11. The angle between OC and OD (Figure 4d) is $\theta = 2\arctan(CM/OM) = 2\arctan(1/(3\sqrt{3})) = 21.79°$, which is equal to the twist angle measured from Figure 4a. The twist angles in Figures 4b and 4c can be obtained using the same method. It should be noted that such SAED patterns in Figures 4a, 4b, and 4c can be observed only when specimen is thin enough and the twist angle exactly matches that in the CSL theory.

The CSL boundaries with distinct Σ values in two-dimensional α-Fe_2O_3 nanoblades provide a good system to investigate the effects of different grain boundaries on their physical properties. Figure 5a shows a nanoblade with a CSL boundary, which has an average length of 230 nm and an average width of 430 nm. SAED study shows that no Fe or other iron oxides are left on the nanoblade when scraped off the substrate. To obtain more reliable results, we have performed the electrical property measurement of 3 or 5 individual nanoblades for each kind CLS boundary. All the linear $I-V$ curves for nanoblades with different Σ values in Figure 5b demonstrate metallic characteristics, which show significant difference with previous studies on Fe_2O_3 nanowires.[22] The resistance of the nanoblade can be measured from the $I-V$ curves, and then the electrical resistivities of the nanoblades can be calculated using eq 2.

$$\rho = \frac{SR}{L} \qquad (2)$$

In this equation, ρ represents electrical resistivity, R is resistance, and L and S are the length and cross-sectional area of the nanoblade, respectively. The average electrical resistivities for three different kinds of nanoblades are calculated to be $(8.8 \pm 0.5) \times 10^{-5}$, $(6.9 \pm 0.4) \times 10^{-5}$, and
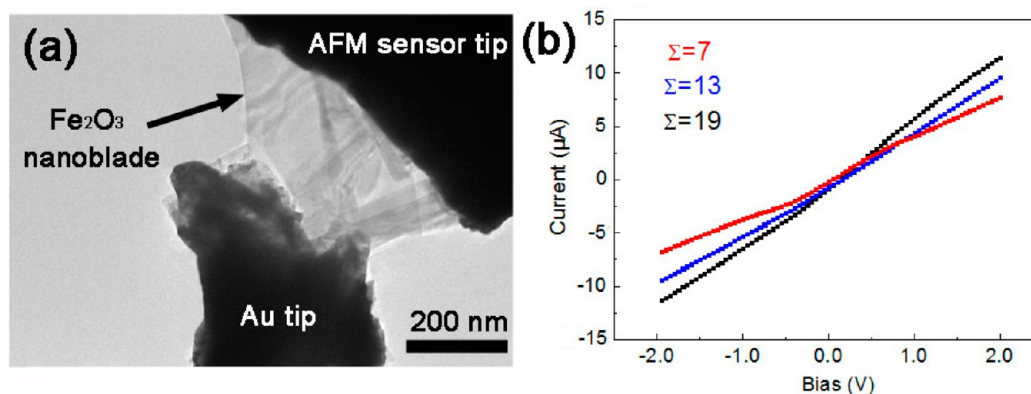
Figure 5. (a) BF TEM image of single α-Fe$_2$O$_3$ nanoblade in contact with two electrodes. (b) *In situ* measured *I*−*V* curves for nanoblades with different CSL boundaries.

$(5.6 \pm 0.4) \times 10^{-5}$ $\Omega\cdot$cm, which show drastic decreases compared with nanowires ($\rho = 4.42 \times 10^3$ $\Omega\cdot$cm)[22] and bulk α-Fe$_2$O$_3$ ($\rho = 2.29 \times 10^8$ $\Omega\cdot$cm).[23] This drastic difference can be explained by the CSL boundary plane, which can be regarded as a thin two-dimensional nanosheet,[24] providing good channels for electrons to pass through and thus enhancing the conductivity of the nanoblade. The plot of resistivity versus Σ values is shown in Figure S12, from which it can be clearly seen that the resistivity of the nanoblade decreases with the increase of Σ value. The higher Σ value, the more disordered atomic arrangement at the boundary, which might provide more channels for electrons to pass through and result in better conductivity. Such two-dimensional nanomaterials may have practical appeal because their two-dimensional geometries facilitate integration into devices with realistic pathways to manufacturing.[25]

4. CONCLUSIONS

In conclusion, bicrystalline α-Fe$_2$O$_3$ nanoblades have been synthesized through oxidation of sandblasted Fe foils. TEM examination of individual nanoblades demonstrates that all the bicrystalline nanoblades possess CSL boundaries with only three distinct Σ values of 9, 13, and 19. Statistical analysis shows these CSL boundaries have a volume percentage of 60%, 30%, and 10%, respectively. A simple geometric pattern composed of regular hexagons is employed to describe the rotation angles which lead to the formation of CSL twist boundaries for rotations about [0001] in hcp crystals. The resistivity of the nanoblade decreases with the increase of the Σ value of the CSL boundary.

ASSOCIATED CONTENT

Ⓢ Supporting Information

Figures showing schematic diagram of *in situ* measurement, XRD pattern, EELS spectra, atomic model, simulated HRTEM images, hexagonal network pattern and resistivity as a function of Σ value of Fe$_2$O$_3$ nanoblades. This material is available free of charge via the Internet at http://pubs.acs.org.

AUTHOR INFORMATION

Corresponding Author

*Ph +86 532 83780318; e-mail yqwang@qdu.edu.cn (Y.W.).

Author Contributions

Y.W. and C.W. contributed equally to this work.

REFERENCES

(1) Lu, K.; Lu, L.; Suresh, S. Strengthening Materials by Engineering Coherent Internal Boundaries at the Nanoscale. *Science* **2009**, *324*, 349−352.

(2) Tan, L.; Sridharan, K.; Allen, T. R.; Nanstad, R. K.; McClintock, D. A. Microstructure Tailoring for Property Improvements by Grain Boundary Engineering. *J. Nucl. Mater.* **2008**, *374*, 270−280.

(3) Watanabe, T. Grain Boundary Engineering: Historical Perspective and Future Prospects. *J. Mater. Sci.* **2011**, *46*, 4095−4115.

(4) Randle, V. *The Role of the Coincidence Site Lattice in Grain Boundary Engineering*; Maney: London, UK, 1996.

(5) Kronberg, M. L.; Wilson, F. H. Secondary Recrystallization in Copper. *Trans. AIME* **1949**, *185*, 501−514.

(6) Lin, P.; Palumbo, G.; Harase, J.; Aust, K. T. Coincidence Site Lattice (CSL) Grain Boundaries and Goss Texture Development in Fe-3% Si Alloy. *Acta Mater.* **1996**, *44*, 4677−4683.

(7) Gertsman, V. Y.; Bruemmer, S. M. Study of Grain Boundary Character along Intergranular Stress Corrosion Crack Paths in Austenitic Alloys. *Acta Mater.* **2001**, *49*, 1589−1598.

(8) Chun, H.; Na, S. M.; Mudivarthi, C.; Flatau, A. B. The Role of Misorientation and Coincident Site Lattice Boundaries in Goss-Textured Galfenol Rolled Sheet. *J. Appl. Phys.* **2010**, *107*, 09A960.

(9) Saylor, D. M.; Rohrer, G. S. Measuring the Influence of Grain-Boundary Misorientation on Thermal Groove Geometry in Ceramic Polycrystals. *J. Am. Ceram. Soc.* **1999**, *82*, 1529−1536.

(10) Carlsson, J. M.; Ghiringhelli, L. M.; Fasolion, A. Theory and Hierarchical Calculations of the Structure and Energetics of [0001] Tilt Grain Boundaries in Graphene. *Phys. Rev. B* **2011**, *84*, 165423.

(11) Yazyev, O. V.; Louie, S. G. Electronic Transport in Polycrystalline Graphene. *Nat. Mater.* **2010**, *9*, 806−809.

(12) Huang, P. Y.; Ruiz-Vargas, C. S.; van der Zande, A. M.; Whitney, W. S.; Levendorf, M. P.; Kevek, J. W.; Garg, S.; Alden, J. S.; Hustedt, C. J.; Zhu, Y.; et al. Grains and Grain Boundaries in Single-Layer Graphene Atomic Patchwork Quilts. *Nature* **2011**, *469*, 389−392.

(13) Sato, Y.; Yamamoto, T.; Ikuhara, Y. Atomic Structures and Electrical Properties of ZnO Grain Boundaries. *J. Am. Ceram. Soc.* **2007**, *90*, 337−357.

(14) Cheng, C. L.; He, J. L.; Hu, J. Naturally Asymmetrical Double-Schottky Barrier Model: Based on Observation of Bicrystal. *Appl. Phys. Lett.* **2012**, *101*, 173508.

(15) Yuan, L.; Wang, Y. Q.; Cai, R. S.; Jiang, Q. K.; Wang, J. B.; Li, B. Q.; Sharma, A.; Zhou, G. W. The Origin of Hematite Nanowire Growth during the Thermal Oxidation of Iron. *Mater. Sci. Eng., B* **2012**, *177*, 327−336.

(16) Yuan, L.; Cai, R. S.; Jang, J. I.; Zhu, W. H.; Wang, C.; Wang, Y. Q.; Zhou, G. W. Morphological Transformation of Hematite Nanostructures. *Nanoscale* **2013**, *5*, 7581−7588.

(17) Hirsch, P.; Howie, A.; Nicholson, R. B.; Pashley, D. W.; Whelan, M. J.; Robert, E. *Electron Microscopy of Thin Crystals*; Krieger: Huntington, NY, 1977.

(18) Oba, F.; Ohta, H.; Sato, Y.; Hosono, H.; Yamamoto, T.; Ikuhara, Y. Atomic Structure of [0001]-Tilt Grain Boundaries in ZnO: a High-Resolution TEM Study of Fiber-Textured Thin Films. *Phys. Rev. B* **2004**, *70*, 125415.

(19) Ruterana, P.; Abouzaid, M.; Béré, A.; Chen, J. Formation of a Low Energy Grain Boundary in ZnO: the Structure Unit Concept in Hexagonal Symmetry Materials. *J. Appl. Phys.* **2008**, *103*, 033501.

(20) Warrington, D. H. The Coincidence Site Lattice (CSL) and Grain Boundary (DSC) Dislocations for the Hexagonal Lattice. *J. Phys. Colloq.* **1975**, *36*, C4-87−C4-95.

(21) Brokman, A.; Balluffi, R. W. Coincidence Lattice Model for the Structure and Energy of Grain Boundaries. *Acta Metall.* **1981**, *29*, 1703−1719.

(22) Hsu, L. C.; Li, Y. Y.; Hsiao, C. Y. Synthesis, Electrical Measurement, and Field Emission Properties of α-Fe_2O_3 Nanowires. *Nanoscale Res. Lett.* **2008**, *3*, 330−337.

(23) Sarangi, P. P.; Vadera, S. R.; Patra, M. K.; Prakash, C.; Ghosh, N. N. DC Electrical Resistivity and Magnetic Property of Single-Phase α-Fe_2O_3 Nanopowder Synthesized by a Simple Chemical Method. *J. Am. Ceram. Soc.* **2009**, *92*, 2425−2428.

(24) Balendhran, S.; Deng, J.; Ou, J. Z.; Walia, S.; Scott, J.; Tang, J.; Wang, K. L.; Field, M. R.; Russo, S.; Zhuiykov, S.; et al. Enhanced Charge Carrier Mobility in Two-Dimensional High Dielectric Molybdenum Oxide. *Adv. Mater.* **2013**, *25*, 109−114.

(25) Rogers, J. A.; Lagally, M. G.; Nuzzo, R. G. Synthesis, Assembly and Applications of Semiconductor Nanomembranes. *Nature* **2011**, *477*, 45−53.